Structure



# Super-resolution imaging reveals cytoskeleton-dependent organelle rearrangement within platelets at intermediate stages of maturation

## Graphical abstract

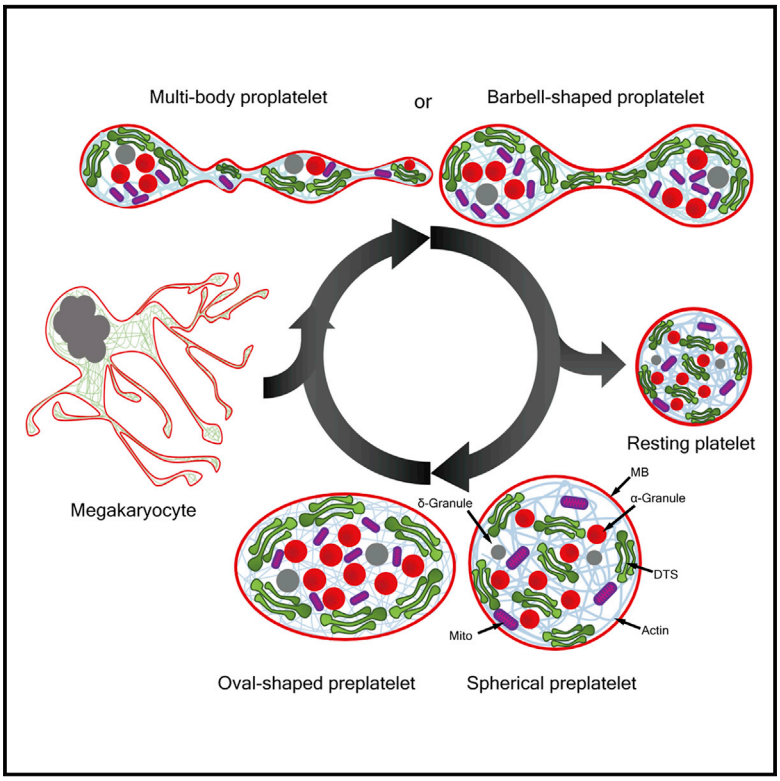


## Highlights

- Super-resolution microscopy resolves the ultrastructures in platelet intermediates
- Platelet intermediates are reversibly converted to each other via various pathways
- Number of mitochondria increase in the intermediate steps of platelet maturation
- Distribution of organelles in platelet intermediates are regulated by cytoskeleton

## Authors

Seokran Go, Dokyung Jeong, Jinkyoung Chung, ..., Eunyoung Moon, Yang Hoon Huh, Doory Kim

## Correspondence

doorykim@hanyang.ac.kr

## In brief

Go et al. propose that the platelet intermediates increase their protein contents to prepare their maturation and gradually distribute them with the help of cytoskeletal elements. Once ready for generating platelet progeny, they undergo reversible conversions between the different intermediate states, and finally separate into small resting platelets.

Go et al., 2021, Structure *29*, 810–822
August 5, 2021 
https://doi.org/10.1016/j.str.2021.06.001

CellPress

CellPress

Structure

Article

# Super-resolution imaging reveals cytoskeleton-dependent organelle rearrangement within platelets at intermediate stages of maturation

Seokran Go,[1] Dokyung Jeong,[1] Jinkyoung Chung,[1] Geun-ho Kim,[1] Jaewoo Song,[2] Eunyoung Moon,[3] Yang Hoon Huh,[3] and Doory Kim[1,4,5,6,7,*]

[1]Department of Chemistry, Hanyang University, Seoul 04763, Republic of Korea
[2]Department of Laboratory Medicine, Yonsei University College of Medicine, Seoul 03722, Republic of Korea
[3]Electron Microscopy Research Center, Korea Basic Science Institute, Cheongju 28119, Republic of Korea
[4]Research Institute for Convergence of Basic Sciences, Hanyang University, Seoul 04763, Republic of Korea
[5]Institute of Nano Science and Technology, Hanyang University, Seoul 04763, Republic of Korea
[6]Research Institute for Natural Sciences, Hanyang University, Seoul 04763, Republic of Korea
[7]Lead contact
*Correspondence: doorykim@hanyang.ac.kr
https://doi.org/10.1016/j.str.2021.06.001

## SUMMARY

A steady supply of platelets maintains their levels in the blood, and this is achieved by the generation of progeny from platelet intermediates. Using systematic super-resolution microscopy, we examine the ultrastructural organization of various organelles in different platelet intermediates to understand the mechanism of organelle redistribution and sorting in platelet intermediate maturation as the early step of platelet progeny production. We observe the dynamic interconversion between the intermediates and find that microtubules are responsible for controlling the overall shape of platelet intermediates. Super-resolution images show that most of the organelles are located near the cell periphery in oval preplatelets and confined to the bulbous tips in proplatelets. We also find that the distribution of the dense tubular system and α granules is regulated by actin, whereas that of mitochondria and dense granules is governed by microtubules. Altogether, our results call for a reassessment of organelle redistribution in platelet intermediates.

## INTRODUCTION

Platelets are anucleated blood cells derived from megakaryocytes in the bone marrow. Their main function is to contribute to hemostasis and, therefore, a steady supply of platelets supports their levels in the blood. Recent studies have demonstrated that platelet number increases during platelet storage because platelets can generate progeny (Richardson et al., 2005; Schwertz et al., 2010; Thon and Italiano, 2010; Thon et al., 2010); newly formed platelets are functionally and structurally indistinguishable from normal platelets (Schwertz et al., 2010). A better understanding of the mechanisms underlying platelet progeny generation could improve therapies for thrombocytopenia and thrombocytosis (Thon and Italiano, 2010). However, the mechanisms underlying platelet progeny generation through the maturation of platelet intermediates that power and regulate organelle distribution remain unknown. To improve therapies for disorders related to platelet number, such as thrombocytopenia and thrombocytosis, elucidating these mechanisms has been an important research goal for this field, in addition to defining the biological pathways that control the production of platelets from megakaryocytes (Richardson et al., 2005; Schwertz et al., 2010; Thon and Italiano, 2010; Thon et al., 2010).

Two major models have been proposed for the mechanism underlying platelet production and release: the cytoplasmic fragmentation model and the proplatelet model (Richardson et al., 2005). According to the cytoplasmic fragmentation model, organelles are pre-packaged within the body of the megakaryocyte. In contrast, the proplatelet model hypothesizes that the entire megakaryocyte cytoplasm is remodeled into proplatelets. Two intermediate stages of platelet production have been recently identified in support of this model: proplatelets and preplatelets (Italiano Jr et al., 2007; Richardson et al., 2005; Thon and Italiano, 2010, 2012; Thon et al., 2012). Proplatelets slowly mature into multiple individual platelets that contain all the materials and programming required to synthesize and release functional progeny. Proplatelets can be reversibly converted to recently defined intermediate structures called preplatelets that have a discoid shape with prominent cortical microtubule bundles. These intermediate structures are known to be responsible for regulating platelet size (Thon et al., 2010, 2012). During this process, a mechanism underlying organelle redistribution and sorting may be involved before platelet release.

Several studies have attempted to investigate this mechanism by monitoring the distribution and dynamics of organelles (Richardson et al., 2005; Thon et al., 2010). However, the

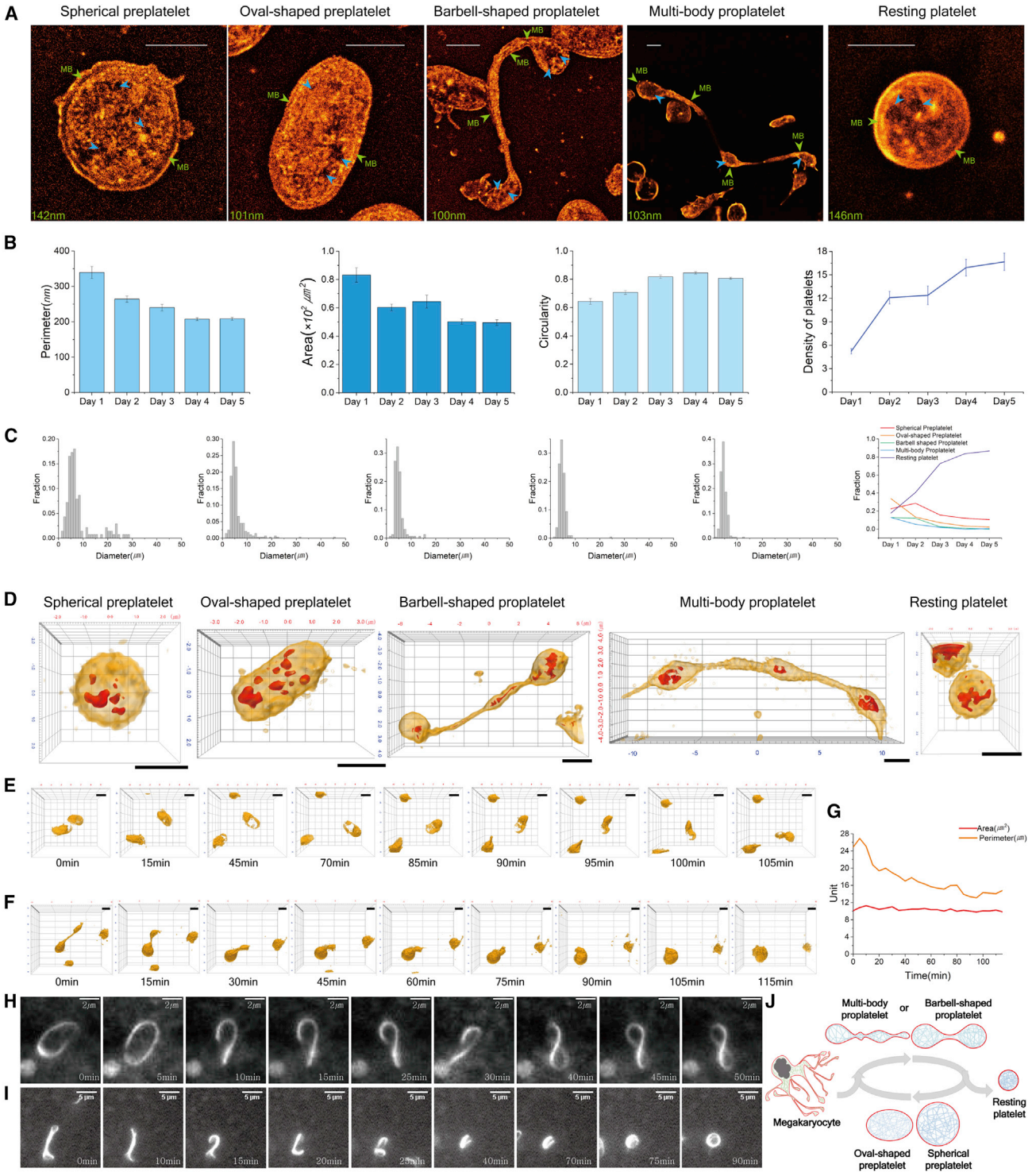


**Figure 1. Various platelet intermediate stages and their interconversion**

(A) Representative 2D STORM images of a Nile red-labeled platelet in the distinct stages of platelet (green arrows: marginal band of microtubules [MB], blue arrows: open canalicular system [OCS]).

(B) The bar graphs indicate the cell perimeter, area, circularity, and number (from left to right) of platelets (mean ± SD; n = 183) after 1–5 days in culture.

(C) Relative distribution of intermediates as a function of their longest diameter at different culture days (left five images) and the relative intermediate count for each platelet intermediate after 1–5 days in culture (right).

*(legend continued on next page)*

distribution and dynamics of organelles in other intermediate forms during platelet maturation remain unknown due to the technical challenge of obtaining the ultrastructure of small-sized platelets with conventional microscopy techniques. Difficulty in determining and quantifying the ultrastructure of platelets arises from the limited resolution of traditional light microscopy and the limited specific labeling efficiency of electron microscopy (EM). These limitations can be overcome with recent advances in super-resolution fluorescence microscopy (Hell, 2007; Huang et al., 2010; Rust et al., 2006).

By taking advantage of super-resolution fluorescence microscopy, we have identified several organelle interactions in different intermediate stages of proplatelet maturation and investigated the interconversion mechanism between different intermediates that control platelet release. Using stochastic optical reconstruction microscopy (STORM), we also demonstrated that actin and microtubules had differential influence on organelle distribution in proplatelets. To conduct a systematic microscopic study of platelet release, we used a combination of live-cell three-dimensional (3D) optical diffraction tomography, live-cell fluorescence imaging, transmission electron microscopy (TEM), and high-voltage EM (HV-EM). A systematic series of state-of-the-art microscopy provided insights into organelle distribution during the interconversion process between the different intermediates of platelet production.

## RESULTS

### Observation of platelet intermediates and their live-cell imaging

To observe the various types of platelet intermediates, we performed STORM imaging of platelet-rich plasma (PRP) after 2 days in culture because we could see various platelet intermediates on these days as shown in Figure 1C. To observe the overall shape of platelet intermediates, we used Nile red as a lipid stain that has recently been demonstrated for super-resolution imaging of membranes (Moon et al., 2017). The STORM images showed the diverse morphology of platelets, such as resting platelets, circular preplatelets, oval preplatelets, barbell-shaped proplatelets, and multi-body proplatelets (Figure 1A). We confirmed that the spherical shapes in the Nile red-negative region in the middle of the platelet are the vacant space within the open canalicular system (OCS) by observing the open surface area of the OCS from the 3D STORM images of Nile red-stained resting and activated platelets (Figure S1). The marginal band (MB) of the microtubules was visualized as the Nile red-negative space because only membrane structures can be labeled with Nile red staining and that MB is a non-membranous structure. In particular, the space for the MB was thinner in a barbell-shaped proplatelet than in a resting platelet, probably due to the spread of the peripheral microtubule bundle ring along the boundary of the extended length in a barbell-shaped proplatelet. To distinguish intermediates of platelet production, we performed quantitative analysis of the identified platelets from differential interference contrast images. During the culture period, the total number and circularity of platelets increased, whereas the perimeter and area of platelets decreased, indicating platelet release into the culture (Figure 1B). Based on their perimeter, area, and circularity measurements, the cells were categorized as multi-body proplatelets, barbell-shaped proplatelets, circular-shaped preplatelets, or resting platelets. We used the ~3-μm threshold as the minimum diameter for preplatelets, as reported previously (Thon et al., 2012). The preplatelets with a longer diameter had an oval shape, whereas those with a shorter diameter had a spherical shape. Preplatelets with diameters longer than 5 μm were rarely detected, and platelets with diameters longer than 8 μm had at least two cell bodies that identified them as proplatelets. Among the proplatelets, multi-body proplatelets with a diameter longer than 12 μm consisted of more than three or more cell bodies. Under this categorization, we found that the fraction of multi-body proplatelets and barbell-shaped proplatelets decreased, whereas the fraction of circular preplatelets and resting platelets increased during the culture period (Figure 1C). Collectively, we found that platelets in our cultures generated new cell bodies and increased in number.

To further investigate the conversion between the observed platelet intermediates, we next examined the changes in platelet morphology by using 3D optical diffraction tomography, which measures the 3D refractive index (RI) distribution of samples. Although this technique is a label-free method, the tomograms of platelets obtained with RI showed several organelles rendered as red objects, such as protein clusters in various platelet intermediates, which suggested the presence of granules (Figure 1D). The 3D holographic movies of living platelets revealed that proplatelets are dynamic intermediate stages (Figures 1E and 1F). We observed that some of the preplatelets convert to proplatelets via twisting (Figure 1E; Video S1); however, only a few of these preplatelets converted into barbell-shaped proplatelets by overcoming the resistance to elastic bending force, while most preplatelets returned to their original oval shape. Interestingly, we also observed that some of the proplatelets converted into preplatelets via absorption of one of the two bodies over a period of 105 min, which has not been reported previously (Figure 1F; Video S2). During the conversion from proplatelets to preplatelets via absorption, the cell perimeter decreased even though the cell area remained constant (Figure 1G). These results suggested that there were more densely packed peripheral microtubules in preplatelets than in proplatelets, which is consistent with our previous observation of MB thickness in these two platelet intermediates. This observation suggests the reversible capacity of proplatelet-to-preplatelet conversion via multiple mechanisms.

(D–F) (D) Representative 3D optical diffraction tomograms of platelets in distinct stages of platelet production. The red objects with a high refractive index value are considered to be protein clusters, such as granules. 3D optical diffraction tomography time-lapse sequence showing (E) the conversion from a preplatelet to a twisted proplatelet and (F) the conversion from a barbell-shaped proplatelet to a preplatelet without splitting (5 min per snapshot).

(G–I) (G) The changes in area and perimeter of the platelet intermediates during the conversion from barbell-shaped proplatelets to preplatelets observed in (F). Fluorescence live-cell imaging of (H) an SiR-tubulin-labeled platelet showing the conversion from an oval preplatelet to a proplatelet via twisting of MB, and (I) the conversion from a barbell-shaped proplatelet to a resting platelet via folding.

(J) Schematic diagram showing the interconversion between the different platelet intermediates and platelet progeny production. Scale bar, 2 μm.

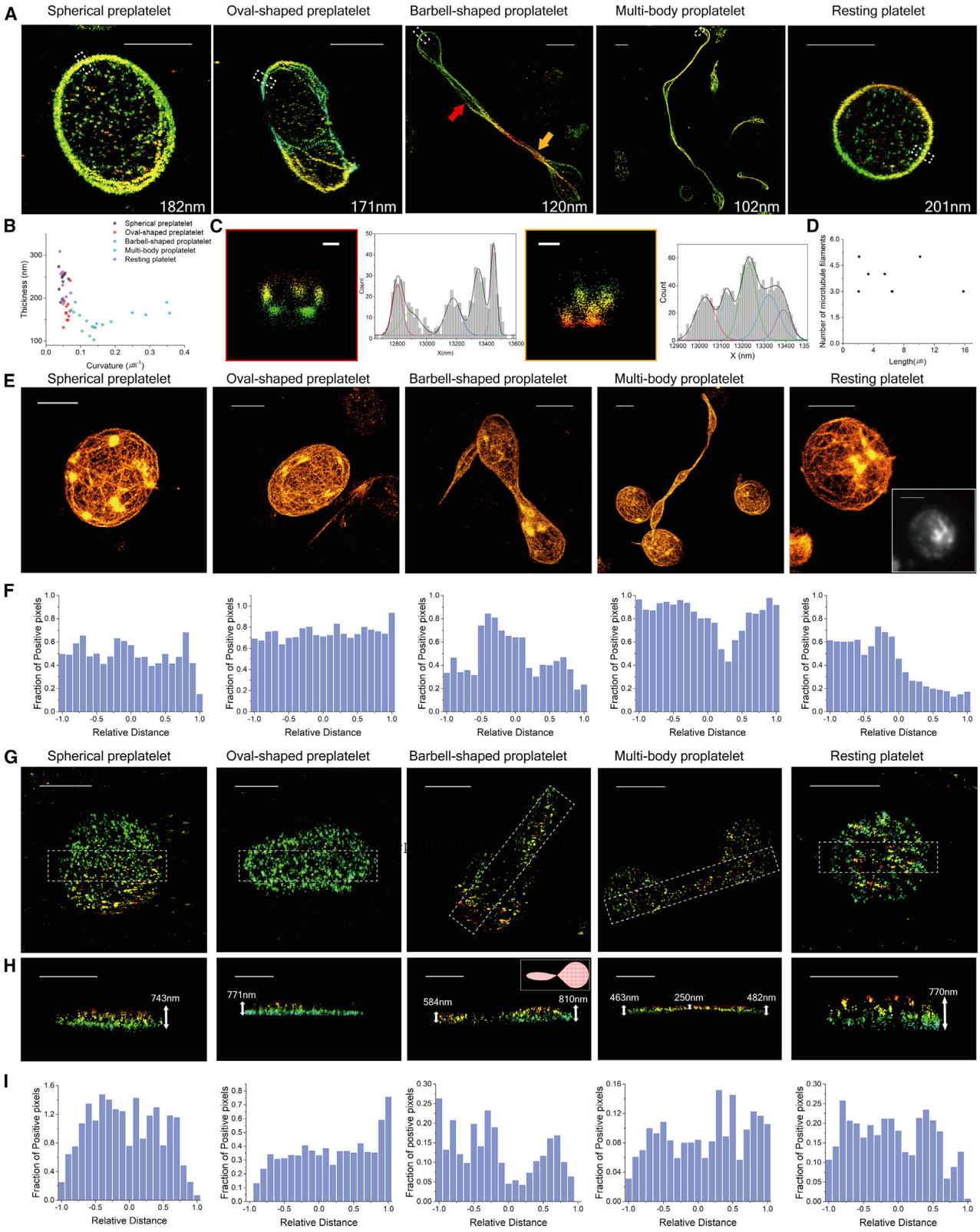


**Figure 2. STORM images of cytoskeletal elements in platelet intermediates**

(A) Representative 3D STORM images of microtubules in platelets during the distinct stages of platelet production.

(B) Curvature/thickness measurements of barbell-shaped proplatelets (n = 52).

*(legend continued on next page)*

We next performed fluorescence live-cell imaging of microtubules in platelets to observe the dynamics of MB in the conversion process of platelet intermediates. The live fluorescence images showed various reversible conversions between preplatelets and proplatelets, similar to 3D holographic imaging. For example, we observed the conversion from oval preplatelets to proplatelets via MB twisting (Figure 1H; Video S3). As we observed in the 3D holographic movie, the live fluorescence images showed that only a few such preplatelets (18.9%) were observed to convert into barbell-shaped proplatelets by overcoming the resistance to elastic bending force, although many of them were observed to twist (33.3%). We also observed that the oval preplatelets, in which the microtubules were disrupted by nocodazole drug treatment for 15 min, showed a lower rate of the complete conversion (4.5%) to barbell-shaped proplatelets than the non-treated oval preplatelets (18.9%), probably due to the role of MB in the conversion to barbell-shaped proplatelets (Figure S2). These results are consistent with those of previous studies, in which the conversion from the preplatelet to the barbell-shaped proplatelet based on twisting was likely to be regulated by the microtubule bundle (Thon and Italiano, 2012; Thon et al., 2010, 2012). Interestingly, the conversion from the barbell-shaped proplatelet to the resting platelet via folding was also observed (1.47%), which, to the best of our knowledge, has not been reported to date (Figure 1I; Video S4). Thus, it is likely that the platelet intermediates are dynamic and can be interconverted to each form through different mechanisms (Figure 1J).

## Super-resolution imaging of cytoskeletal elements in platelet intermediates

The results from live-cell imaging suggested that cytoskeletal elements play an important role in maintaining the morphology of platelets during platelet production because the interconversion between oval preplatelets and barbell-shaped proplatelets is likely to be regulated by peripheral MB thickness. Therefore, we resolved the ultrastructural changes of microtubule organization during proplatelet maturation using STORM. Using immunolabeling of the microtubules, we observed the microtubule structure at the nanoscale. The 3D STORM results indicated that the thickness of the peripheral MB increased from 120 to 201 nm during the conversion from a barbell-shaped proplatelet to a resting circular platelet, which was consistent with our membrane-staining imaging (Figure 2A). To further illustrate the relationship of MB thickness and the curvature of the platelet body, we quantified these factors from STORM images of different platelet intermediates. The quantification results showed that the thickness and curvature of peripheral microtubule coils were anticorrelated (Figure 2B). Moreover, from the microtubule perturbation experiment using nocodazole treatment, we observed that the spherical shape of the resting platelets was converted to a spiky shape, and that the curvatures of platelet intermediates increased after nocodazole treatment by losing the rigidity of the spherical shape (Figure S3). These results suggest that the MB thickness regulated their shape and rigidity. The thinner peripheral microtubule coils in barbell-shaped proplatelets were able to overcome the resistance to elastic bending forces with high curvature. Interestingly, the twisting of the microtubules along a bridge length of 11 μm was observed in barbell-shaped proplatelets, which has not been previously resolved in three dimensions due to diffraction-limited imaging methods (Thon et al., 2010, 2012). From the cross-section, five microtubules were clearly resolved in the barbell-shaped proplatelet shaft with a twisting diameter of 500–800 nm (Figure 2C). The twisting of the microtubules in the barbell-shaped proplatelet shaft likely lowered the resistance to elastic bending forces at the end of the shaft. We also found no correlation between the length of the shaft and the number of microtubule filaments. We also found that at least three microtubules were needed to form the bridge (Figure 2D). Therefore, this result suggests that the conversion between preplatelets and proplatelets is driven by the reorganization of microtubule filaments.

We next performed STORM imaging of actin in the platelet intermediates. In contrast to the conventional images of actin structures, individual actin filaments were clearly resolved in the STORM images (Figure 2E). We observed a dense actin meshwork in all platelet intermediates, whereas actin bundles were rarely observed. Quantitative analysis of spatial density showed a consistently dense and homogeneous actin meshwork with similar spatial density of actin between the bridge and the two-body regions, suggesting no significant role of actin in the integrity of the cytoplasmic bridge between the platelet-sized ends (Figure 2F). We also found that the actin nodules disappeared in one platelet body in some of the multi-body proplatelets. Given that actin nodules can link adhesion sites to the cytoskeleton, the platelet progeny body newly formed from the mother body might have flexible dynamics without strong adhesion rather than actin nodules (Poulter et al., 2015). Moreover, we observed actin filaments in the protrusion but not microtubules in the STORM images of the protrusion, indicating that they are likely composed of actin filaments (Figure S4).

We next investigated the 3D localization of spectrin-based membrane cytoskeletons using 3D STORM. Since it has been recently suggested that the spectrin-actin-based cortical cytoskeletons in intact erythrocytes reveal a meshwork with nanoscale voids, we tried to investigate whether such a spectrin organization is also shown in the various types of platelet intermediates (Pan et al., 2018). We used an anti-β2-spectrin

(C) The x-z cross-section of the 3D STORM image (left) and the distribution profiles for two points along the x-z cross-section (right; red and yellow arrows, respectively) in (A). Each histogram is fit to 5 Gaussians (red curves).
(D) The number of microtubule filaments/length of cytoplasmic bridge measurements from barbell-shaped proplatelets (n = 7).
(E) Representative 2D STORM images of actin in platelets in the distinct stages of platelet production. Inset: diffraction-limited conventional fluorescence image of a resting platelet.
(F) The radial distribution graph of actin in the platelet shown in (E).
(G) Representative 3D STORM images of β2-spectrin in platelets in the distinct stages of platelet production (from left to right): spherical preplatelet, oval-shaped preplatelet, barbell-shaped proplatelet, multi-body proplatelet, and resting platelet.
(H) The x-z cross-section of the 3D STORM image shown in the white dashed box of (G). Inset in 3D STORM image: schematic representation showing a "twisted barbell-shaped proplatelet."
(I) The radial distribution graph of β2-spectrin in the platelet shown in (G). Scale bar, 2 μm.

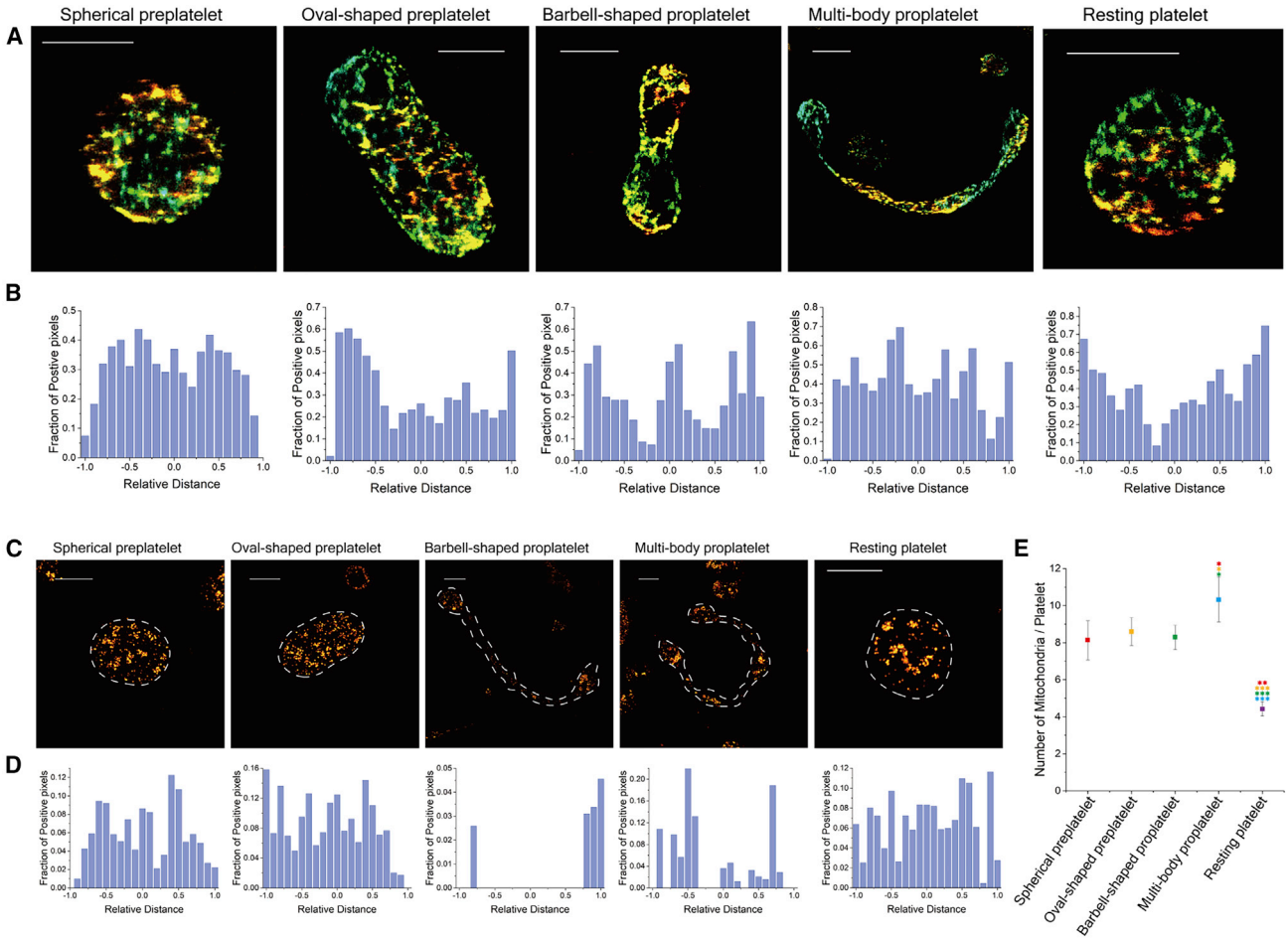


**Figure 3. STORM images of double membrane-bound organelles**

(A) Representative 3D STORM images of DTS in platelets in the distinct stages of platelet production.

(B) The radial distribution graph of DTS of the platelet shown in (A).

(C) Representative 3D STORM images of mitochondria in the distinct platelet intermediates.

(D) The radial distribution graph of mitochondria in the platelet shown in (C).

(E) The average mitochondria number per platelet in each distinct stage of platelet production (mean ± SD, n = 53; *p < 0.05, **p < 0.01, ***p < 0.001). Scale bar, 2 μm.

antibody because β2-spectrin is the major spectrin isoform in platelets (Patel-Hett et al., 2011). The 3D STORM images of β2-spectrin revealed a uniform distribution along the whole length of the platelet body that had a punctate and speckled pattern similar to β2-spectrin distribution in the erythrocyte cytoskeleton (Figure 2G) (Pan et al., 2018). From the x-z cross-section of the 3D STORM images, we also observed that the β2-spectrin cytoskeletal layer rose in height at the cell center outside of the focal range in resting platelets, while the membrane cytoskeleton in oval preplatelets and proplatelets was flat down, which has not been previously seen (Figure 2H). Previous studies have shown that the spectrin-based membrane skeleton stabilizes membrane systems in mouse megakaryocytes and is essential for maintaining proplatelet structure (Patel-Hett et al., 2011). The spectrin-based membrane cytoskeleton also lines the inner plasma membrane and crosslinks long actin filaments to form networks (Heijnen and Korporaal, 2017). This is supported by our observation of a similar homogeneous distribution of actin and β2-spectrin over the length of the platelet intermediate body (Figure 2I). This homogeneously distributed β2-spectrin-based membrane skeleton suggests that it provides structural integrity to the cell that preserves the long shape of proplatelet architecture.

## Super-resolution imaging of double membrane-bound organelles

To understand how different organelles are distributed over the whole cell area of different platelet intermediates, we imaged double membrane-bound organelles, such as the dense tubular system (DTS) and mitochondria, using STORM. The DTS represents the smooth ER in platelets and acts as a calcium store for membrane fusion events and cell activation (Heijnen and Korporaal, 2017). Super-resolution images revealed a homogeneously distributed DTS in the form of a membrane network, which has not been clearly resolved from the previous TEM section imaging (Figure 3A). These tubular, vesicular membrane structures of the

DTS were consistent with the intertwined structure observed in electron tomography images in previous studies (van Nispen tot Pannerden et al., 2010). In the middle of platelet intermediates, a few small, empty spaces were often observed, some of which appeared to be closely associated with the OCS, where it may contribute to the local release of calcium to the OCS as part of extracellular signaling pathways (Heijnen and Korporaal, 2017; van Nispen tot Pannerden et al., 2010). Notably, the DTS membranes were positioned close to the plasma membrane in preplatelets and barbell-shaped proplatelets and appeared to prepare them for division. Density distribution analysis along the longest length of the platelet intermediates illustrated the membrane-associated position of the DTS in the barbell-shaped proplatelets (Figure 3B). In addition, the density in the cytoplasmic bridge between the bodies was relatively high, which could be due to their role in synthesizing phospholipids as in plasma membranes. This high density of DTS in the cytoplasmic bridge was maintained even after the two bodies were separated (Figure S5).

We also examined the ultrastructural distribution of mitochondria in platelet intermediates using STORM. STORM images of mitochondria showed that there were four mitochondria on average homogeneously distributed as small punctate foci throughout a resting platelet cell, which was consistent with previous reports (Figures 3C and 3D) (Heijnen and Korporaal, 2017). The quantification analysis showed that the number of mitochondria increases in the preplatelets and proplatelets compared with that in the resting platelets, suggesting that there were newly synthesized proteins during the conversion between the different platelet intermediates (Figure 3E). Interestingly, the homogeneously distributed mitochondria in resting platelets moved to the plasma membrane in oval preplatelets and were confined to the bulbous tips of the barbell-shaped proplatelets, which had significantly low mitochondrial density along the cytoplasmic bridge. Previous studies have suggested that the mitochondria found along the bridge could be translocating along the length of proplatelets (Richardson et al., 2005). However, a very low density of mitochondria in the bridge (11% on average) was observed in our analysis of the STORM images and, hence, the transportation process through the bridge is not likely a major mechanism used to distribute mitochondria into the two platelet bodies. Our observations suggest that most mitochondria are distributed on both sides of the platelet-sized swellings in oval preplatelets, and only a small number of mitochondria are transported through the cytoplasmic bridge into the barbell-shaped proplatelets if needed.

## Super-resolution imaging of secretory vesicles

We next investigated the ultrastructural distribution of secretory organelles in platelet intermediates using STORM. Among the four types of secretory organelles, we performed STORM imaging of $\alpha$ granules and dense granules, which are the major secretory organelles known to play crucial roles in secondary platelet response (van Nispen tot Pannerden et al., 2010). The $\alpha$ granules were highly variable in their morphology and size, with spherical $\alpha$ granules being the predominant morphology observed, which was consistent with previous reports (Figure 4A) (van Nispen tot Pannerden et al., 2010). To quantify $\alpha$ granules from STORM images, we set the diameter of the cluster to 200 nm, which was the minimum size criterion to distinguish the $\alpha$ granules from a non-specific single antibody-binding signal. With this criterion, the average number of $\alpha$ granules was six, and the average $\alpha$ granule area was 0.03–0.07 $\mu m^2$ in resting platelets, which was consistent with a previous study (Rumbaut and Thiagarajan, 2010). Interestingly, distribution analysis showed that $\alpha$ granules localized to the periphery of the cell as the length of the platelet intermediates increased (Figure 4B). In particular, $\alpha$ granules were confined to the platelet-sized swellings in tandem arrays, but not in the connecting cytoplasmic bridges in the multi-body proplatelets. Such distribution was observed consistently from the STORM images of platelet intermediates regardless of the culture day (Figure S6). The distribution of $\alpha$ granules appeared to be similar to that of mitochondria; therefore, the transportation process via the bridge was not a likely mechanism for $\alpha$ granule distribution in platelet-sized swellings. Moreover, the distribution of most $\alpha$ granules to both sides of the platelet-sized swellings in oval preplatelets had already begun.

We next observed dense granule distribution in the platelet intermediates. The dense granules were exhibited as small punctate foci with an average number of three in a platelet and an average diameter of 140 nm, which was consistent with previous observations (Figure 4C) (Rumbaut and Thiagarajan, 2010). Although their distribution pattern was not clearly observed due to their low density, our quantitative analysis indicated that they were homogeneously distributed in resting platelets (Figure 4D). In contrast to resting platelets, the diffuse localization of dense granules was observed in the cytoplasmic bridge, whereas a comparable number of dense granules was distributed to the platelet-sized swellings in barbell-shaped and multi-body proplatelets. These observations were consistent with the previous report of equal movement of secretory granules in both directions along the proplatelet cell (Richardson et al., 2005).

## EM imaging of platelet intermediates

Collectively, we observed that most of the organelles in platelet intermediates were already distributed to both sides of oval-shaped preplatelets before conversion to proplatelets, and they were almost equally localized to both sides of barbell-shaped proplatelets (Figure 5A). To examine the distribution of the different organelles together, we performed EM imaging. The HV-EM images of spherical preplatelets showed that most organelles localized far from the center of the cells (Figure 5B; Video S5). In particular, DTS showed a clear peripheral distribution when compared with the other organelles. We also observed this peripheral distribution in TEM images of the different platelet intermediates (Figure 5C). The peripheral distribution of DTS was clearly observed in oval-shaped preplatelets, and most of the organelles were confined to the platelet-sized swellings in multi-body proplatelets. TEM imaging also revealed that the organelles moved to the peripheral region of platelet intermediates in the order of DTS, secretory vesicles, and mitochondria. This order could be one reason why a previous study reported that mitochondria were transported through the bridge in barbell-shaped proplatelets (Richardson et al., 2005).

## Effect of cytoskeletal elements on organelle distribution

Based on the super-resolution fluorescence and EM images and distribution analysis results of different organelles in platelet intermediates, we found that most of the organelles were

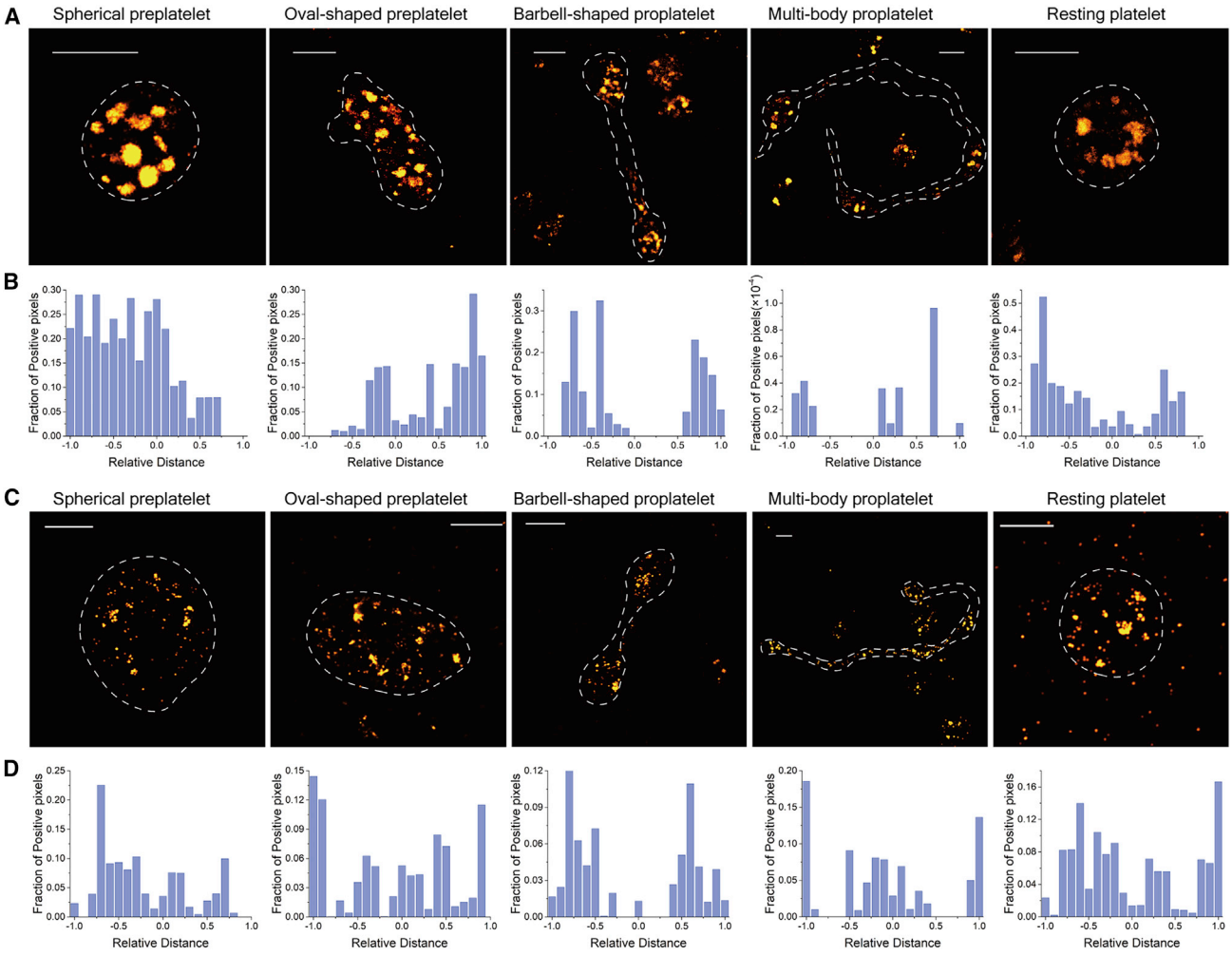


**Figure 4. STORM images of secretory vesicles**

(A) Representative 3D STORM images of α granules in spherical preplatelets, oval-shaped preplatelets, barbell-shaped proplatelets, multi-body proplatelets, and resting platelets (from left to right).

(B) The radial distribution graph of α granules in the platelet shown in (A).

(C) Representative 3D STORM images of dense granules in the distinct platelet intermediates.

(D) The radial distribution graph of dense granules in the platelet shown in (C). Scale bar, 2 μm.

homogeneously distributed in resting platelets and peripherally distributed in oval-shaped preplatelets. We also observed that organelles were equally distributed across the platelet-sized swellings in barbell-shaped and multi-body proplatelets with low density in the cytoplasmic bridge, except for DTS, which had a high density in the cytoplasmic bridge. These observations raise questions on how these organelles can be distributed during the interconversion between different platelet intermediates. Previous studies suggest that cytoskeletal mechanisms could be responsible for regulating organelle distribution, but the detailed mechanism is still unknown (Richardson et al., 2005). To test if the cytoskeleton is responsible for organelle distribution, we investigated the effect of cytochalasin D and nocodazole, which disrupt actin and microtubules, respectively, on organelle distribution in different platelet intermediates.

First, we observed a marked contrast in the distribution of organelles in platelets treated with cytochalasin D. For example, α granules had a biased distribution in some of the barbell-shaped proplatelets such that only one side of the bulbous tip was filled with α granules, while the other side of the tip was not (Figures 6A–6C). Although the extent of their biased distribution was highly variable, the calculation of their density difference between the two sides of the tips clearly shows a biased α granule density (average density difference = 0.38) on one side of a tip when compared with the control sample (average density difference = 0.19; Figure 6D). The wide variety in their distribution could be from the different transportation states of proplatelets. For example, the α granules may still show equal distribution in the proplatelet tips if the cells were treated with cytochalasin D after α granule distribution is complete. In contrast, if the cells were treated with cytochalasin D before organelle transportation, it could lead to a biased distribution of α granules on one side of the tips. Furthermore, these biased distributions of organelles after cytochalasin D treatment were observed for DTS, which also

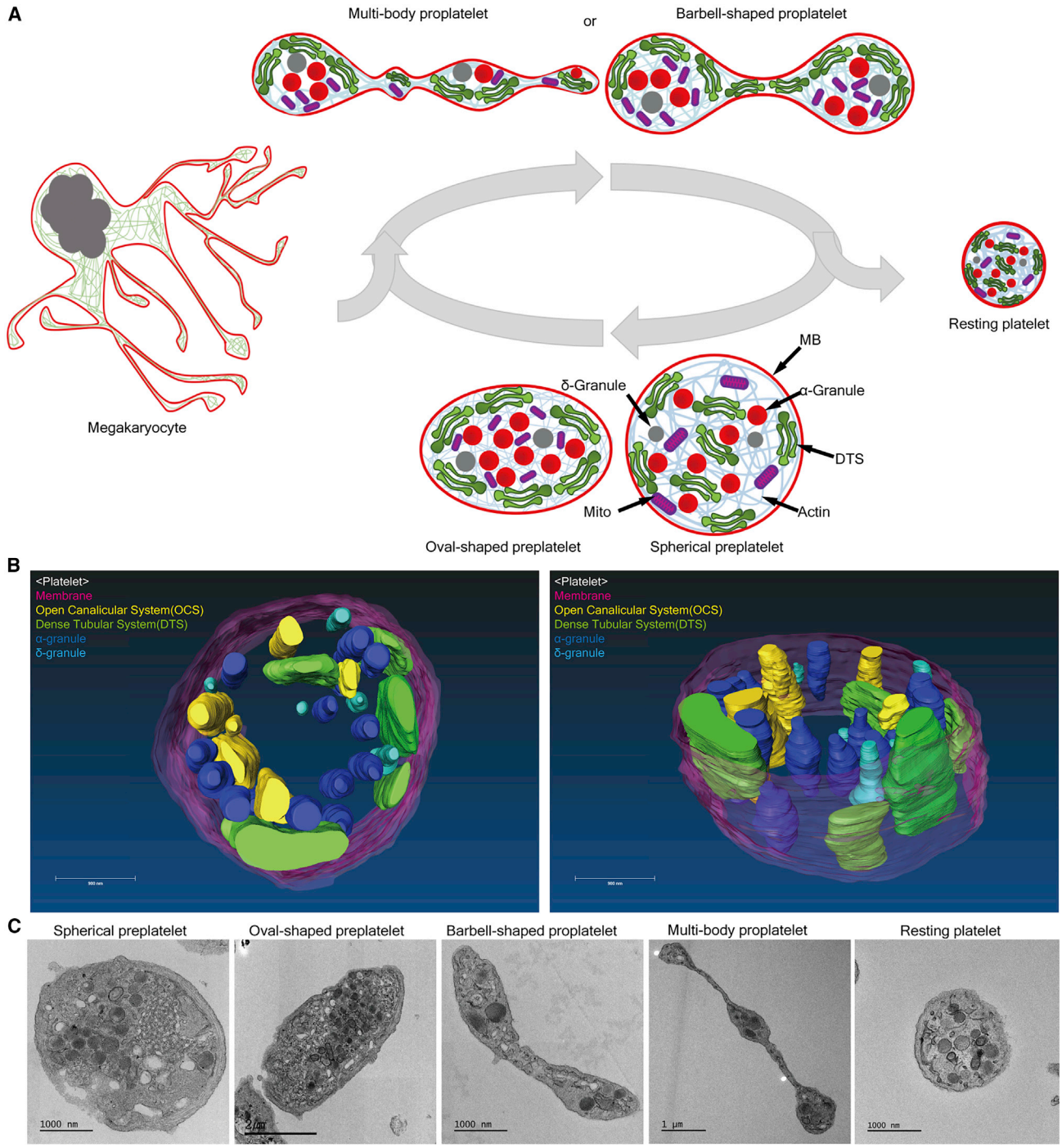


**Figure 5. EM images of platelet intermediates**

(A) Schematic diagram showing the rearrangement of organelles in the different platelet intermediates and platelet progeny production.

(B) The 3D reconstructed HV-EM image of a spherical preplatelet visualized at different angles. Scale bar, 900 nm.

(C) Representative TEM images of the distinct platelet intermediates.

localized to one side of the tips of barbell-shaped proplatelets after cytochalasin D treatment. TEM imaging also showed that the DTS was densely localized on one side of the bulbous tips, whereas α granules were mainly confined to both sides of the tips.

Next, we treated the platelets with nocodazole to disrupt microtubule polymerization. From STORM and TEM imaging, we found that mitochondria and dense granules had biased distributions in some of the barbell-shaped proplatelets such that the organelles localized to only one side of the bulbous tip. In

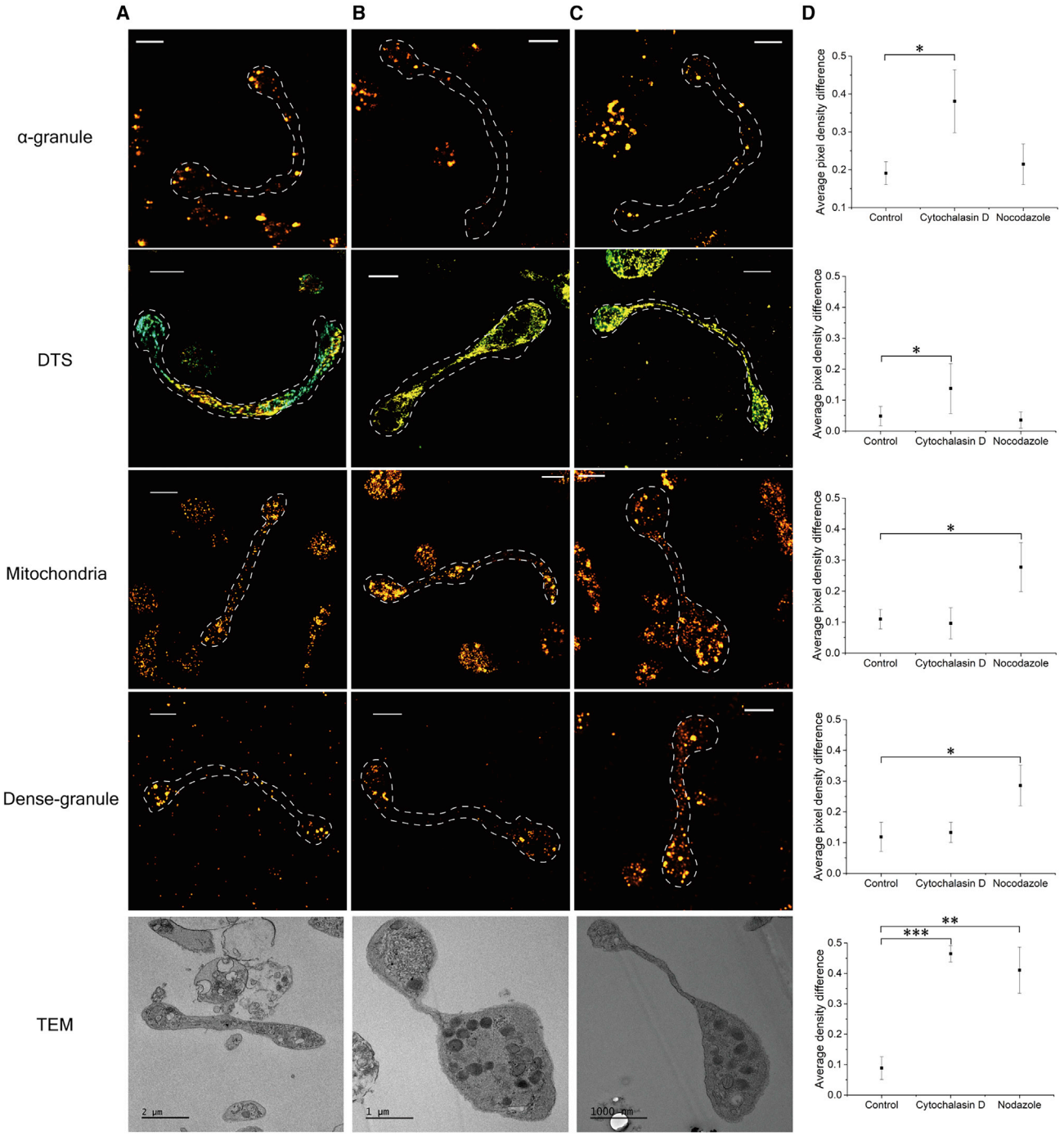


**Figure 6. Effect of cytoskeletal elements on organelle distribution**

(A–C) Representative STORM images of α granules, DTS, mitochondria, and dense granules in (A) control-, (B) cytochalasin D-, or (C) nocodazole-treated barbell-shaped proplatelets.

(D) Average pixel density difference between two sides of the barbell-shaped proplatelet for the different organelles in the STORM images (A–C) and for the secretory granules in the TEM images (n = 5–11; *p < 0.05, **p < 0.01, ***p < 0.001). Scale bar, 2 μm.

contrast, we observed similar distributions of α granules and DTS in nocodazole-treated barbell-shaped proplatelets and control samples, which suggested that their transportation was not guided by microtubules (Figures 6A–6C). The calculation of their density differences in the two sides of the tips showed a biased density (average density difference = 0.28 for mitochondria and 0.29 for dense granules) for mitochondria and dense granules, which was different from the control sample (average density difference = 0.11 for mitochondria and 0.12 for dense granules; Figure 6D). Collectively, our findings suggest that actin

plays an important role in guiding the homogeneous distribution of α granules and the DTS, while microtubules drive the homogeneous distribution of dense granules and mitochondria during the conversion between preplatelets and proplatelets.

## DISCUSSION

Using systematic and integrative super-resolution microscopy, we have uncovered the ultrastructural changes in platelet intermediates during this process by characterizing the ultrastructural organization and relative arrangements of various organelles in different platelet intermediates.

Our live-cell imaging showed the dynamic and reversible conversion between proplatelets and preplatelets via various pathways, including folding, twisting, and merging of two bodies. Such a reversible conversion has not been visualized before in real time, although it was suspected in the previous model (Thon et al., 2010). Our study demonstrates significant, yet previously overlooked, interconversion dynamics between platelet intermediates before the production of platelet progeny. In particular, we observed (1) that barbell-shaped proplatelets could fold into small preplatelets and (2) that one of the two bodies was absorbed into the other body. These hypotheses explain the conversion mechanisms from proplatelet to preplatelet without fission. It was relatively difficult to capture the fission process of the proplatelet conversion into preplatelets under our experimental conditions. It is possible that such an abscission process is too rapid to be readily captured or that circulatory shear stresses in the blood stream are required to separate these bodies (Thon et al., 2010, 2012). Instead of this abscission process, the interconversion between the platelet intermediates appears to be a frequent dynamic process that sets the equilibrium between two states depending on the need for functional platelets.

Using super-resolution microscopy, we observed multiple intermediate stages in platelet production, including resting platelets, circular preplatelets, oval-shaped preplatelets, barbell-shaped proplatelets, and multi-body proplatelets, all of which were consistent with the intermediates previously identified during platelet production (Richardson et al., 2005; Thon and Italiano, 2010). In this study, we visualized the nanoscale ultrastructures of different organelles in various platelet intermediate stages for the first time using super-resolution microscopy. The spectrin-actin-based submembrane cytoskeleton showed homogeneous distribution over the whole body of platelet intermediates, potentially to maintain the structure and integrity of the surface membrane in the platelet intermediates. In addition, we could observe actin filaments in the protrusion, which probably acts as a sensor to probe the environment for adhesion. In contrast, microtubules remained at the boundary of the platelet intermediates, with the thickness of the microtubule bundle closely related to the curvature of the membrane boundary, which suggests that the microtubules are responsible for controlling the overall shape of platelet intermediates. In particular, we resolved the twisted shape of thin cytoplasmic bridges in barbell-shaped proplatelets, which appeared to be responsible for the balance between the elastic bending force of the bundling and twisting forces. Super-resolution images of microtubules revealed that there were at least three microtubules in the cytoplasmic bridge of barbell-shaped proplatelets, which seems to be the minimal bundling force needed to resist the circular shape of the two-sided bodies in proplatelets.

We also conducted super-resolution imaging of double membrane-bound organelles and secretory vesicles in different platelet intermediates. First of all, we found that the number of mitochondria increases in the platelet intermediates relative to the resting platelet, probably implying the need for protein synthesis in the platelet intermediates before converting to a resting state. Although the protein synthesis in platelets has attracted considerable interest and has been investigated using activated platelets, the observation of the increased protein contents in the platelet intermediates at the single platelet level has not been reported yet (Weyrich et al., 2009). Given that mitochondria are primarily responsible for the function and survival of platelets, and finally determining platelet lifespan, the need for mitochondria may increase in the intermediate steps of platelet maturation up to twice the amount in resting platelets (Hwa et al., 2019).

From the distributions of double membrane-bound organelles and secretory vesicles in different platelet intermediates, we observed that they showed a relatively higher density near the cell periphery than in the center in oval preplatelets and were confined to the bulbous tips of barbell-shaped proplatelets, which contrasts the observation of actin and spectrin localization. We also found that mitochondria, α granules, and dense granules had significantly low density along the cytoplasmic bridge in the barbell-shaped proplatelets, which was also different from that of actin and spectrin. However, DTS showed clear localization close to the plasma membrane with high density in the cytoplasmic bridge in the barbell-shaped proplatelets, which appeared to maintain the plasma membrane integrity of the barbell-shaped proplatelets.

These observations raise questions on how these organelles can be distributed during the interconversion between different platelet intermediates. Previous studies suggest that cytoskeletal mechanisms could be responsible for regulating organelle distribution, but the detailed mechanism for the various organelles' rearrangements during maturation remains unknown (Richardson et al., 2005). Results with the nocodazole-treated platelet intermediates support the importance of microtubules in the transportation of mitochondria and dense granules into barbell-shaped proplatelets. In contrast, actin disruption by cytochalasin D led to a biased distribution of DTS and α granules in one of the two bodies of the barbell-shaped proplatelets, but not that of mitochondria and dense granules. Therefore, the distribution of DTS and α granules was governed by actin, while that of mitochondria and dense granules was governed by microtubules. Our results, however, are different from those of a previous study that suggested the microtubule-based long-distance transport of organelles along proplatelets based on the observation of mitochondrial transportation in live platelets (Richardson et al., 2005). A reason for this disparity may be the difference in transportation mechanisms observed between the previous study and the current study. While in the previous study, the mitochondrial transportation process was observed in established barbell-shaped proplatelets, in this study, we observed their distribution at the cell periphery in oval preplatelets before their conversion to proplatelets. This stage occurs earlier than that observed in the previous study. Therefore, we suggest

that there are several transport mechanisms for organelles, as also suspected by the previous study (Richardson et al., 2005); one pertains to transportation before the barbell-shaped proplatelet is established, whereas the other process occurs after the coil of a proplatelet is established.

Collectively, our findings highlight an unexpected, diverse mechanism for the distribution of organelles in different platelet intermediates and point to the significant, yet previously overlooked interconversion mechanisms between the different intermediates in the platelet progeny production process. Based on our observations, we propose that the platelet intermediates increase their protein contents using their protein synthesis machinery to prepare their maturation and gradually distribute them equally into two-sided swellings of proplatelet with the help of cytoskeletal elements. Once they are ready for generating platelet progeny, they would undergo the reversible conversions between the different intermediate states via various pathways depending on the need for resting platelets in our body, and finally separated into small-sized resting platelets. We anticipate that these techniques will shed light on the fundamental molecular mechanisms of platelet structure and function. We expect that further studies utilizing live-cell super-resolution fluorescence microscopy, such as live-cell STORM/structured illumination microscopy/stimulated emission depletion microscopy, would be valuable for directly visualizing organelle redistributions in platelet intermediates in real time. Moreover, in the case of 3D super-resolution imaging of the volumetric morphology of thick platelet intermediates, such as the twisted oval preplatelet, the use of a self-bending point spread function or double-helix PSF would be helpful (Jia et al., 2014; Pavani et al., 2009; Quirin et al., 2012; Schroeder and Jia, 2015). Ultimately, a better understanding of the molecular mechanisms of platelet formation will lead to improved therapies for disorders related to platelet number, such as thrombocytopenia and thrombocytosis.

## STAR★METHODS

Detailed methods are provided in the online version of this paper and include the following:

- KEY RESOURCES TABLE
- RESOURCE AVAILABILITY
  - Lead contact
  - Materials availability
  - Data and code availability
- EXPERIMENTAL MODEL AND SUBJECT DETAILS
  - Cell culture
- METHOD DETAILS
  - Live platelet imaging
  - Sample preparation for STORM imaging
  - STORM imaging
  - EM imaging
- QUANTIFICATION AND STATISTICAL ANALYSIS
  - Quantification of STORM data

## SUPPLEMENTAL INFORMATION

Supplemental information can be found online at https://doi.org/10.1016/j.str.2021.06.001.

## ACKNOWLEDGMENTS

This work was supported by the National Research Foundation of Korea (NRF) grant funded by the Korea government (MSIT) (no. 2018R1C1B6003436), the POSCO Cheongam Foundation (Fellowship to D.K.), the Korea Basic Science Institute under the R&D program (project no. C030440) supervised by the Ministry of Science and ICT, and the Bio & Medical Technology Development Program of the National Research Foundation (NRF) funded by the Ministry of Science & ICT (no. 2017M3A9G8084539). We also thank Z. Gerelkhuu and T. Yoon for discussion.

## AUTHOR CONTRIBUTIONS

S.G. participated in all experimental work, analyzed data, and contributed to both artwork design and manuscript writing. D.J., J.C., and G.K. contributed to work related to the STORM imaging. J.S. provided PRP samples. E.M. and Y.H.H. performed the TEM imaging. E.M. performed the HV-EM imaging. S.G., D.J., and D.K. wrote, reviewed, and edited the paper. D.K. supervised, conceived the work, designed the research studies, wrote original draft, and performed the final editing of paper. All authors reviewed the paper.

## DECLARATION OF INTERESTS

The authors declare no competing interests.

Received: January 19, 2021
Revised: March 27, 2021
Accepted: May 28, 2021
Published: June 17, 2021

## REFERENCES

Chan, C.Y., Pedley, A.M., Kim, D., Xia, C., Zhuang, X., and Benkovic, S.J. (2018). Microtubule-directed transport of purine metabolons drives their cytosolic transit to mitochondria. PNAS *115*, 13009–13014.

French, J.B., Jones, S.A., Deng, H., Pedley, A.M., Kim, D., Chan, C.Y., Hu, H., Pugh, R.J., Zhao, H., and Zhang, Y. (2016). Spatial colocalization and functional link of purinosomes with mitochondria. Science *351*, 733–737.

Fukami, M., Bauer, J., Stewart, G., and Salganicoff, L. (1978). An improved method for the isolation of dense storage granules from human platelets. J. Cell Biol. *77*, 389–399.

Heijnen, H.F., and Korporaal, S.J. (2017). Platelet morphology and ultrastructure. In Platelets in Thrombotic and Non-thrombotic Disorders, P. Gresele, N. Kleiman, J. Lopez, and C. Page, eds. (Springer), pp. 21–37.

Hell, S.W. (2007). Far-field optical nanoscopy. science *316*, 1153–1158.

Huang, B., Babcock, H., and Zhuang, X. (2010). Breaking the diffraction barrier: super-resolution imaging of cells. Cell *143*, 1047–1058.

Hwa, J., Melchinger, H., Jain, K., and TYAGI, T. (2019). Role of platelet mitochondria: life in a nucleus-free zone. Front. Cardiovasc. Med. *6*, 153.

Italiano Jr, J., Patel-Hett, S., and Hartwig, J. (2007). Mechanics of proplatelet elaboration. J. Thromb. Haemost. *5*, 18–23.

Jia, S., Vaughan, J.C., and Zhuang, X. (2014). Isotropic three-dimensional super-resolution imaging with a self-bending point spread function. Nat. Photon. *8*, 302–306.

Kim, D., Deerinck, T.J., Sigal, Y.M., Babcock, H.P., Ellisman, M.H., and Zhuang, X. (2015). Correlative stochastic optical reconstruction microscopy and electron microscopy. PLoS One *10*, e0124581.

Moon, S., Yan, R., Kenny, S.J., Shyu, Y., Xiang, L., Li, W., and Xu, K. (2017). Spectrally resolved, functional super-resolution microscopy reveals nanoscale compositional heterogeneity in live-cell membranes. J. Am. Chem. Soc. *139*, 10944–10947.

Pan, L., Yan, R., Li, W., and Xu, K. (2018). Super-resolution microscopy reveals the native ultrastructure of the erythrocyte cytoskeleton. Cell Rep. *22*, 1151–1158.

Patel-Hett, S., Wang, H., Begonja, A.J., Thon, J.N., Alden, E.C., Wandersee, N.J., An, X., Mohandas, N., Hartwig, J.H., and Italiano, J.E., Jr. (2011). The

spectrin-based membrane skeleton stabilizes mouse megakaryocyte membrane systems and is essential for proplatelet and platelet formation. Blood *118*, 1641–1652.

Pavani, S.R.P., Thompson, M.A., Biteen, J.S., Lord, S.J., Liu, N., Twieg, R.J., Piestun, R., and Moerner, W. (2009). Three-dimensional, single-molecule fluorescence imaging beyond the diffraction limit by using a double-helix point spread function. PNAS *106*, 2995–2999.

Poulter, N.S., Pollitt, A.Y., Davies, A., Malinova, D., Nash, G.B., Hannon, M.J., Pikramenou, Z., Rappoport, J.Z., Hartwig, J.H., and Owen, D.M. (2015). Platelet actin nodules are podosome-like structures dependent on Wiskott-Aldrich syndrome protein and ARP2/3 complex. Nat. Commun. *6*, 1–15.

Quirin, S., Pavani, S.R.P., and Piestun, R. (2012). Optimal 3D single-molecule localization for superresolution microscopy with aberrations and engineered point spread functions. PNAS *109*, 675–679.

Richardson, J.L., Shivdasani, R.A., Boers, C., Hartwig, J.H., and Italiano, J.E., Jr. (2005). Mechanisms of organelle transport and capture along proplatelets during platelet production. Blood *106*, 4066–4075.

Rumbaut, R.E., and Thiagarajan, P. (2010). Platelet-vessel wall interactions in hemostasis and thrombosis. Synthesis lectures on integrated systems physiology: From molecule to function. Function *2*, 1–75.

Rust, M.J., Bates, M., and Zhuang, X. (2006). Sub-diffraction-limit imaging by stochastic optical reconstruction microscopy (STORM). Nat. Methods *3*, 793–796.

Schroeder, B., and Jia, S. (2015). Frequency analysis of a self-bending point spread function for 3D localization-based optical microscopy. Opt. Lett. *40*, 3189–3192.

Schwertz, H., Köster, S., Kahr, W.H., Michetti, N., Kraemer, B.F., Weitz, D.A., Blaylock, R.C., Kraiss, L.W., Greinacher, A., and Zimmerman, G.A. (2010). Anucleate platelets generate progeny. Blood *115*, 3801–3809.

Stenina, O.I., and Plow, E.F. (2008). Counterbalancing forces: what is thrombospondin-1 doing in atherosclerotic lesions? Circ. Res. *103*, 1053–1055.

Thon, J.N., and Italiano, J.E. (2010). Platelet formation. Semin. Hematol. *47*, 220–226.

Thon, J.N., and Italiano, J.E., Jr. (2012). Does size matter in platelet production? Blood *120*, 1552–1561.

Thon, J.N., Macleod, H., Begonja, A.J., Zhu, J., Lee, K.-C., Mogilner, A., Hartwig, J.H., and Italiano, J.E. (2012). Microtubule and cortical forces determine platelet size during vascular platelet production. Nat. Commun. *3*, 1–9.

Thon, J.N., Montalvo, A., Patel-Hett, S., Devine, M.T., Richardson, J.L., Ehrlicher, A., Larson, M.K., Hoffmeister, K., Hartwig, J.H., and Italiano, J.E., Jr. (2010). Cytoskeletal mechanics of proplatelet maturation and platelet release. J. Cell Biol. *191*, 861–874.

van Nispen tot Pannerden, H., de Haas, F., Geerts, W., Posthuma, G., van Dijk, S., and Heijnen, H.F. (2010). The platelet interior revisited: electron tomography reveals tubular α-granule subtypes. Blood *116*, 1147–1156.

Weyrich, A.S., Schwertz, H., Kraiss, L.W., and Zimmerman, G.A. (2009). Protein synthesis by platelets: historical and new perspectives. J. Thromb. Haemost. *7*, 241–246.

## STAR★METHODS

### KEY RESOURCES TABLE

| REAGENT or RESOURCE | SOURCE | IDENTIFIER |
|---|---|---|
| **Antibodies** | | |
| Rat monoclonal anti-α-tubulin | Abcam | Cat#ab6160; RRID: AB_305328 |
| Mouse monoclonal anti-β2-spectrin | BD Biosciences | Cat#612562; RRID: AB_399853 |
| Mouse monoclonal anti-thrombospondin 1 | Invitrogen | Cat#MA5-13398; RRID: AB_10984611 |
| Rat monoclonal anti-serotonin | Abcam | Cat#ab6336; RRID: AB_449517 |
| Mouse monoclonal anti-Tom20 (F-10) | Santa Cruz Biotechnology | Cat#sc-17764; RRID: AB_628381 |
| Rabbit polyclonal anti-Tom22 | Abcam | Cat#ab246862 |
| Rabbit monoclonal anti-KLC3 | Abcam | Cat#ab180523 |
| Goat anti- Rat | Invitrogen | Cat#A-21247; RRID: AB_141778 |
| Donkey anti- Mouse | Invitrogen | Cat#A-31571; RRID: AB_162542 |
| Donkey anti- Rabbit | Invitrogen | Cat#A31573; RRID: AB_2536183 |
| **Biological samples** | | |
| Blood sample | Hospital of Yonsei University Health System | Approval Number: 4-2012-0336 |
| **Chemicals, peptides, and recombinant proteins** | | |
| SiR-tubulin | CYTOSKELETON, INC. | Cat#CY-SC002 |
| Verapamil | CYTOSKELETON, INC. | Cat#CY-SC002 |
| Paraformaldehyde | Electron Microscopy Sciences | Cat#15714 |
| Glutaldehyde | Electron Microscopy Sciences | Cat#16020 |
| sodium borohydride | Sigma-Aldrich | Cat#71320 |
| Mercaptoethylamine | Sigma-Aldrich | Cat#30070 |
| glucose oxidase | Sigma-Aldrich | Cat#G2133 |
| Catalase | Sigma-Aldrich | Cat#C3515 |
| Alexa Fluor 647-conjugated phalloidin | Invitrogen | Cat#A22287 |
| Nile Red | Acros Organics | Cat#415711000 |
| ascorbic acid | Sigma-Aldrich | Cat#PHR1008 |
| tannic acid | Sigma-Aldrich | Cat#403040 |
| **Software and algorithms** | | |
| TomoStudioTM | Tomocube Inc. | N/A |
| TEM Recorder software | JEOL System Technology | N/A |
| Visualizer-Kai software | Frontiers Inc | TEMography.com |
| AMIRA software | Thermo Fisher Scientific (FEI) | N/A |
| Matlab | MathWorks | N/A |
| **Other** | | |
| Microscope | Nikon | Ti2-U |
| 100 × 1.49 NA oil immersion objective lens | Nikon | CFI SR HP Apo TIRF |
| 561 nm laser | OBIS | Coherent |
| 647 nm laser | OBIS | Coherent |
| 405 nm laser | OBIS | Coherent |
| bandpass emission filter | Semrock | LF408/488/561/635-B |
| EMCCD camera | Andor | iXon Ultra 888 |
| CRISP Autofocus system | Applied Scientific Instrumentation (ASI) | CRISP-890 |
| cylindrical lens | Thorlabs | LJ1144RM-A |
| Field Emission Scanning Electron Microscope | Zeiss | S-4800 |

(*Continued on next page*)

*Continued*

| REAGENT or RESOURCE | SOURCE | IDENTIFIER |
|---|---|---|
| Ultramicrotome | Leica | EM UC7 ultramicrotome |
| Bio-EM System | JEOL | JEM-1400 Plus at 120 kV |
| Bio-HVEM System | JEOL | JEM-1000BEF |

## RESOURCE AVAILABILITY

### Lead contact

Further information and requests for resources and reagents should be directed to and will be fulfilled by the lead contact, Doory Kim (doorykim@hanyang.ac.kr).

### Materials availability

This study did not generate new unique reagents.

### Data and code availability

The Matlab code supporting the current study have been deposited and can be found by using the following link.
https://sites.google.com/hanyang.ac.kr/kim-lab.

## EXPERIMENTAL MODEL AND SUBJECT DETAILS

### Cell culture

This study was approved by the Institutional Review Board (IRB) of Severance Hospital (Seoul, Republic of Korea), an affiliated hospital of Yonsei University Health System (Approval Number: 4-2012-0336). All participants (female: 58%; male: 42%; age: 20–59) provided written informed consent before the donation of blood samples. Blood samples were acquired with the approval of the IRB and all experiments were performed in accordance with relevant guidelines and regulations. To purify the PRP, the blood sample was drawn into sodium citrate tubes and centrifuged at 250 ×*g* for 15 min at room temperature (RT), followed by separation of the supernatant as the PRP. The PRP were then plated onto a glass-bottomed confocal dish that was incubated at 37°C and 5% $CO_2$ after dilution in Dulbecco's phosphate buffered saline (DPBS).

## METHOD DETAILS

### Live platelet imaging

For live-cell imaging of microtubules in platelets, the cell samples were stained with 1 μM SiR-tubulin (CY-SC002; Cytoskeleton) with 10 μM verapamil for 30 min at 37°C and 5% $CO_2$, and then imaged at 10 Hz and excited with a 641 nm solid-state laser. For DIC imaging of live platelets, the PRP was diluted in PBS and cultured as described before the DIC images were obtained at 10 Hz.

For the 3D RI tomogram of live platelets, the PRP was diluted in PBS and cultured on a microscopic dish (TomoDish, Tomocube Inc., Republic of Korea) at 37°C and 5% $CO_2$ and then imaged with a holotomography system (HT-2H, Tomocube Inc.) that performed the multiple 2D holographic imaging at various illumination angles. The 3D RI tomogram was reconstructed and rendered using commercial software (TomoStudioTM, Tomocube Inc.).

### Sample preparation for STORM imaging

The PRP was cultured as described above and fixed in 3% (v/v) PFA (15714; Electron Microscopy Sciences) and 0.1% (v/v) GA (16020; Electron Microscopy Sciences) in PBS for 15 min at RT after 1–2 days in culture because we could see various platelet intermediates on those days based on the observations in Figure 1C. The fixed samples were washed three times with PBS and then reduced with freshly prepared 0.1% (w/v) sodium borohydride (71320; Sigma-Aldrich) in PBS for 7 min to minimize background noise. After washing three times with PBS, the samples were permeabilized with 0.3% Triton X-100 in PBS for 10 min and incubated in blocking buffer (3% [w/v] bovine serum albumin [BSA] in PBS) for 30 min. The samples were stained with primary antibodies in blocking buffer for 1 h at RT, washed with PBS or 0.05% (w/v) Triton X-100 in blocking buffer, and then stained with secondary antibodies in blocking buffer for 1 h. Antibodies used included the following: anti-α-tubulin (ab6160; Abcam), anti-β2-spectrin (612562; BD Biosciences), and anti-thrombospondin 1 (MA5-13398; Invitrogen) for α-granules; anti-serotonin (ab6336; Abcam) for dense granules; anti-Tom20 (F-10) (sc-17764; https://datasheets.scbt.com/sc-17764.pdfSanta Cruz Biotechnology) and anti-Tom22 (ab246862; Abcam) for mitochondria; and anti-KLC3 (ab180523; Abcam) for DTS. To image α-granules, the anti-thrombospondin-1 antibody was used because it is a major constituent of α granules (Stenina and Plow, 2008). For dense granules labeling, we used the anti-serotonin antibody because the dense granules store extremely high concentrations of serotonin (Fukami et al., 1978; Richardson et al., 2005). After incubation with the secondary antibodies, samples were rinsed three times and post-fixed with 2% (v/v) PFA and 0.05% GA in PBS for 10 min at RT, followed by brief washing with PBS. The imaging buffer for STORM was prepared with

100 mM mercaptoethylamine (30070; Sigma-Aldrich), 5% glucose (w/v), and oxygen-scavenging enzymes (0.5 mg/mL glucose oxidase [G2133; Sigma-Aldrich], and 38 μg/mL catalase [C3515; Sigma-Aldrich]) in PBS at pH 8.5.

For actin filament staining, the cultured PRP was washed twice with PBS, fixed, and extracted with 0.3% (v/v) GA and 1% (v/v) Triton X-100 in cytoskeleton buffer (CB, 10 mM MES [2-(N-morpholino)ethanesulfonic acid] buffer, 150 mM NaCl, 5 mM ethylene glycol tetraacetic acid, 5 mM glucose, and 5 mM $MgCl_2$, adjusted with NaOH to a pH of 6.1) for 6 min at RT. Samples were then post-fixed using 2% GA in CB for 20 min. The unreacted aldehyde groups were reduced with freshly prepared 0.1% (w/v) sodium borohydride solution for 10 min. After washing three times with PBS, the samples were stained with Alexa Fluor 647-conjugated phalloidin (A22287; Invitrogen) in PBS overnight at 4°C. The samples were briefly washed once with PBS immediately before STORM imaging and immersed in the aforementioned imaging buffer.

For membrane imaging in platelets, the cultured PRP was fixed and reduced as described, following which it was incubated in 100 nM Nile Red (415711000, Acros Organics) solution in DPBS for 30 min at RT. After washing with PBS twice, the sample was imaged by STORM in an imaging buffer of 100−200 μM ascorbic acid (PHR1008; Sigma-Aldrich) solution in PBS. To observe the large size of the OCS from the activated platelets, 0.1 μg/mL phorbol 12-myristate 13-acetate (P1585; Sigma Aldrich) was added at 37°C and 5% $CO_2$ and the activated platelets were stained with Nile red.

### STORM imaging

For super-resolution imaging, the samples were imaged using a custom-built inverted microscope (Ti2-U; Nikon) equipped with a 100 × and 1.49 NA oil immersion objective lens (CFI SR HP Apo TIRF; Nikon). Wavelengths of 561 nm (OBIS; Coherent, 110 mW) and 647 nm (OBIS; Coherent, 120 mW) were used to excite Alexa Fluor 647 and Nile red, respectively. A 405 nm (OBIS; Coherent, 0.1∼1 mW) laser was also used if needed. The emitted fluorescence from the sample was filtered using a bandpass emission filter (LF408/488/561/635-B; Semrock) and detected using an EMCCD camera (iXon Ultra 888; Andor) at a frame rate of 60–100 Hz. During image acquisition, the focal plane was controlled using the CRISP Autofocus system (ASI). To perform 3D STORM imaging, a cylindrical lens with a focal length of 500 mm (LJ1144RM-A; Thorlabs) was introduced for astigmatism. The separated point spread function of each single molecule in the STORM movie was fitted to a Gaussian function and each centroid position was determined to reconstruct the STORM image as previously described(Chan et al., 2018; French et al., 2016; Kim et al., 2015).

### EM imaging

For SEM imaging, the cultured PRP was first washed twice with PBS, fixed after 1-2 days in culture, and permeabilized with 0.3% (v/v) GA and 1% (v/v) Triton X-100 in CB for 10 min at RT, followed by a second fixation using 2% GA in CB for 20 min. To enhance electron contrast, the samples were then incubated in 0.1% (w/v) tannic acid (403040; Sigma-Aldrich) for 20 min, washed with distilled water for 10 min, and stained with 0.1% to 0.2% (w/v) uranyl acetate for 20 min at RT. Next, the samples were rinsed with distilled water for 10 min and dehydrated using a graded ethanol series and hexamethyldisilazane for 15 min. The dehydrated samples were coated with Pt and imaged using an S-4800 Field Emission Scanning Electron Microscope (Zeiss) at 3 keV.

For TEM imaging, the PRP was first fixed with 2.5% GA in 0.1 M cacodylate buffer (pH 7.4) overnight at 4°C and washed with cacodylate buffer three times, followed by post-fixation with 1-2% osmium tetroxide in 0.1 M cacodylate buffer on ice for 1 h. After washing three times with cacodylate buffer, the samples were dehydrated using a graded ethanol series, infiltrated using progressive incubations with propylene oxide and Epon 812, and finally embedded in 100% Epon 812 resin. We obtained approximately 70 nm ultrathin sections using an EM UC7 ultramicrotome (Leica, Austria) and collected them on 100-150 mesh copper grids. The ultrathin sections on the grids were further stained with uranyl acetate and lead citrate and imaged using the KBSI Bio-EM System (JEM-1400 Plus at 120 kV (JEOL, Japan)).

For HV-EM imaging, the samples were prepared as described but were post-fixed with 1–2% osmium tetroxide and 1.5% potassium ferrocyanide in 0.1 M cacodylate buffer. Thick sections (∼700 nm) were obtained to reconstruct the 3D ultrastructure. These sections were imaged using the KBSI Bio-HVEM System (JEM-1000BEF at 1,000 kV (JEOL, Japan)), and a total of 47 tilt images from +46° to −46° tilting angles in increments of 2° were recorded using TEM Recorder software (JEOL System Technology, Tokyo, Japan). These images were aligned and reconstructed using Composer and Visualizer-Kai software (TEMography.com, system in Frontiers Inc., Tokyo, Japan). We used the AMIRA software (Thermo Fisher Scientific (FEI), Hillsboro, OR) for surface rendering and 3D modeling.

## QUANTIFICATION AND STATISTICAL ANALYSIS

### Quantification of STORM data

To quantify the size, number, and distribution of organelles imaged with STORM, the images were first filtered using median filtering, followed by intensity filtering based on Otsu's thresholding algorithm. The boundaries of each organelle from the filtered images were identified using 8-point connectivity, and their boundaries were dilated by 1 pixel. To generate the density distribution of each organelle, the boundaries and centroids of the platelets were identified using the correlative STORM and DIC images. We determined the Euclidean distances between the centroid of a platelet and particular organelle-containing pixels, which were then used to generate the intracellular distribution density of each organelle. The histograms of the localization were normalized to the area of each radial slice. Student's t test was used to determine the statistical significance between different samples in Figures 3E and 6D (*$p < 0.05$, **$p < 0.01$, ***$p < 0.001$).